JOURNAL OF GEOPHYSICAL RESEARCH, VOL. 114, B02212, doi:10.1029/2008JB006132, 2009

Elastic wave speeds and moduli in polycrystalline ice Ih, sI methane hydrate, and sII methane-ethane hydrate

M. B. Helgerud,[1,2,3] W. F. Waite,[4] S. H. Kirby,[2] and A. Nur[1]

Received 1 October 2008; revised 10 December 2008; accepted 30 December 2008; published 27 February 2009.

[1] We used ultrasonic pulse transmission to measure compressional, P, and shear, S, wave speeds in laboratory-formed polycrystalline ice Ih, sI methane hydrate, and sII methane-ethane hydrate. From the wave speed's linear dependence on temperature and pressure and from the sample's calculated density, we derived expressions for bulk, shear, and compressional wave moduli and Poisson's ratio from −20 to −5°C and 22.4 to 32.8 MPa for ice Ih, −20 to 15°C and 30.5 to 97.7 MPa for sI methane hydrate, and −20 to 10°C and 30.5 to 91.6 MPa for sII methane-ethane hydrate. All three materials had comparable P and S wave speeds and decreasing shear wave speeds with increasing applied pressure. Each material also showed evidence of rapid intergranular bonding, with a corresponding increase in wave speed, in response to pauses in sample deformation. There were also key differences. Resistance to uniaxial compaction, indicated by the pressure required to compact initially porous samples, was significantly lower for ice Ih than for either hydrate. The ice Ih shear modulus decreased with increasing pressure, in contrast to the increase measured in both hydrates.

Citation: Helgerud, M. B., W. F. Waite, S. H. Kirby, and A. Nur (2009), Elastic wave speeds and moduli in polycrystalline ice Ih, sI methane hydrate, and sII methane-ethane hydrate, *J. Geophys. Res.*, *114*, B02212, doi:10.1029/2008JB006132.

1. Introduction

[2] Clathrate hydrates of natural gases, commonly referred to as gas hydrates, are nonstoichiometric crystalline solids composed of "guest" molecules trapped in a hydrogen-bonded water molecule framework [*Sloan and Koh*, 2007]. Natural gas hydrate deposits, containing primarily methane, have been identified worldwide in the sediments of deep inland seas, continental margins and permafrost [*Kvenvolden and Lorenson*, 2001]. Its widespread distribution has spurred interest in gas hydrate as a cause of seafloor instability [e.g., *Kayen and Lee*, 1991, 2002; *McIver*, 1982; *Nixon and Grozic*, 2007], a potential energy source [e.g., *Collett*, 2002; *Holder et al.*, 1984; *Ruppel*, 2007], and as a climate change agent [e.g., *Archer*, 2007; *Dickens et al.*, 1995].

[3] Characterizing natural gas hydrate concentrations and distributions to assess gas hydrate's role in these research themes is a challenge. Gas hydrate deposits extend across hundreds to thousands of square kilometers and can be complexly distributed both vertically and horizontally in the subsurface; therefore, characterizing their extent relies on integrating well log measurements with remote sensing information such as that obtained from seismic techniques [e.g., *Dallimore and Collett*, 2005; *Trehu et al.*, 2004]. Tying elastic measurements, such as sonic logs, seismic or seafloor compliance data, to in situ hydrate content requires knowledge of the elastic properties of pure gas hydrate [e.g., *Chand and Minshull*, 2003; *Chand et al.*, 2006; *Helgerud et al.*, 1999; *Lee and Collett*, 2001; *Lee and Waite*, 2008; *Willoughby et al.*, 2008].

[4] Here we provide a unified analysis of wave speed measurements made at the U.S. Geological Survey facilities in Menlo Park, California, on polycrystalline ice Ih, sI methane hydrate and sII methane-ethane hydrate as functions of temperature and pressure. Detailed description of the ice Ih and sI- and sII-hydrate crystal structures is given by *Sloan and Koh* [2007]. This work updates the wave speed and elastic moduli results for ice Ih [*Helgerud*, 2001; *Helgerud et al.*, 2003a]; updates the wave speed results for sI methane hydrate [*Helgerud*, 2001; *Helgerud et al.*, 2003b; *Waite et al.*, 2000] and sII methane-ethane hydrate [*Helgerud et al.*, 2003b]; and provides temperature and pressure fit equations for the elastic moduli of sI and sII hydrate.

[5] Our results for ice Ih, in addition to their intrinsic value in permafrost and other cold region studies, provide a check on our measurement technique. As an additional check on our gas hydrate results, we compare our results to Brillouin spectroscopy wave speed measurements by *Shimizu et al.* [2002], *Baumert et al.* [2002] and *Kiefte et al.* [1985], both above and below our pressure and temperature test conditions. These comparisons demonstrate the utility of our pressure and temperature fits over a broad range of test conditions.

[6] We also report our observations of rapid (<30 min) intergranular annealing during sample fabrication and recovery. These annealing processes, and the resulting wave

[1]Department of Geophysics, Stanford University, Stanford, California, USA.
[2]U.S. Geological Survey, Menlo Park, California, USA.
[3]Now at ExxonMobil Exploration Company, Houston, Texas, USA.
[4]U.S. Geological Survey, Woods Hole, Massachusetts, USA.

0148-0227/09/2008JB006132$09.00

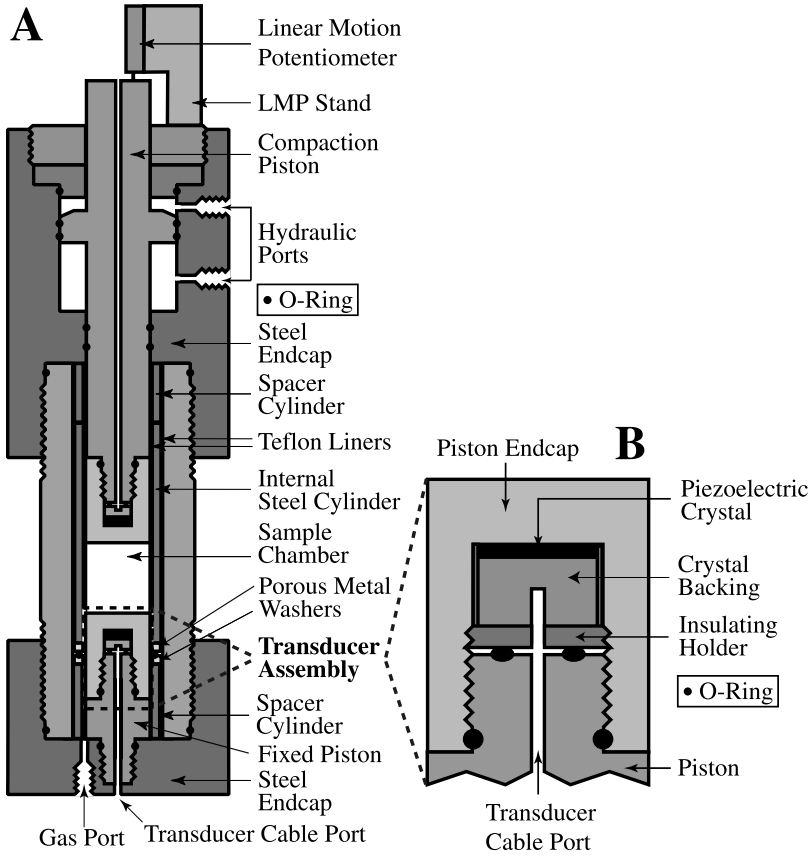

Figure 1. (a) Gas hydrate synthesis and compaction pressure vessel. Sample chamber diameter is 25.4 mm; compacted sample length is ~30 mm. During an experiment, the chamber is suspended in a temperature-controlled bath enclosed in a chest freezer. (b) Transducer assembly, housing a 1 MHz shear crystal coupled to the piston endcap with Panametrics shear couplant.

speed increases, have important consequences for interpreting acoustic results obtained on recovered hydrate-bearing core.

2. Experimental Procedure

2.1. Apparatus

[7] The wave speed measurement pressure vessel consisted of a 25.4 mm diameter sample chamber (Figure 1a) capped by pistons containing 1 MHz center frequency PZT 5A shear wave transducers (Figure 1b). A Panametrics Model 5800 Spike Pulser-Receiver generated shear motion in the upper transducer. The elastic wave traveled through the sample, exciting the lower transducer. If necessary, the signal was passed through a Hewlett Packard 465A amplifier before being displayed on a Tektronix TDS 340 oscilloscope and recorded on a computer.

[8] The upper "compaction" piston was a hydraulic ram, controlled by a Quizix Q-700 metering pump, which provided uniaxial compaction to remove porosity from initially porous granular samples. The Quizix pump also provided a variable load for determining the axial pressure dependence of wave speed. Piston position, and hence the sample length, were continuously monitored by a linear motion potentiometer (LMP) at the top of the pressure vessel.

[9] Pore pressure was adjusted prior to compaction with a gas line linked to the sample chamber through a porous metal ring around the stationary lower piston. The ring was designed to minimize sample extrusion during compaction. To adjust and maintain the sample temperature, the pressure vessel was suspended in a temperature-controlled liquid bath and enclosed in a chest freezer.

2.2. Wave Speed Measurement Technique

[10] Our pulse transmission method of measuring wave speed required simultaneous measurements of the sample length and travel time of an acoustic signal through the sample. Both P and S wave speed, $V_{p,s}$, were calculated from

$$V_{p,s} = \frac{l}{t - t_0} = \frac{l}{t_{p,s}} \tag{1}$$

where l is the sample length, t is the travel time of an acoustic waveform feature with a sample in place, t_0 is the travel time of that same feature when the piston tips were in contact ("head to head" configuration), and $t_{p,s}$ is the true P or S wave travel time in the sample alone.

[11] The sample length, l, was given by the difference in position of the hydraulic piston top (Figure 1) with and without a sample in place. Piston position changes were continually monitored by a linear motion potentiometer (LMP), and checked against periodic measurements of the absolute piston position made with a precision depth

micrometer. We measured the piston position and acoustic travel time in the head-to-head configuration over the pressure and temperature ranges utilized in the experiments to account for length and travel time changes caused by pressure and temperature effects on the vessel and piston assembly.

[12] Low electronic noise levels in the system allowed us to measure both compressional, V_p, and shear, V_s, wave speeds by identifying waveform features from both the precursor P and the S wave generated by the shear wave crystal [*Helgerud*, 2001; *Helgerud et al.*, 2003b]. Tests on an aluminum sample showed the absolute errors due to unidentified systematic errors were less than 1.5% for both V_p and V_s. A detailed description of the waveform feature identification techniques is given by *Helgerud* [2001].

[13] From our simultaneous measurement of compressional and shear waveform travel times, we derived Poisson's ratio, ν:

$$v = \frac{1}{2}\frac{\left(\frac{t_s}{t_p}\right)^2 - 2}{\left(\frac{t_s}{t_p}\right)^2 - 1} = \frac{1}{2}\frac{\left(\frac{V_p}{V_s}\right)^2 - 2}{\left(\frac{V_p}{V_s}\right)^2 - 1}, \quad (2)$$

where t_p and t_s are the P and S waveform travel times, respectively, through the sample.

[14] We applied standard isotropic elasticity relations [*Mavko et al.*, 1998] to determine the dynamic compressional wave (M), bulk (K) and shear (G) moduli of the samples:

$$M = \rho V_p^2 = K + \frac{4}{3}G, \quad (3)$$

$$K = \rho\left(V_p^2 - \frac{4}{3}V_s^2\right), \quad (4)$$

$$G = \rho V_s^2. \quad (5)$$

We conservatively estimated the uncertainty in our density estimate to be 3% (see below). Combining this with our 1.5% uncertainty estimate for the wave speeds, standard error propagation techniques [*Taylor*, 1997] yield an uncertainty of 3% for ν, 4% for M and G, and 6% for K.

[15] The gas hydrate sample density, ρ, in equations (3)–(5) was difficult to measure following an experiment because the sample volume measurement was degraded by cracking and flaking of the hydrate during depressurization and preservation in liquid nitrogen. To obtain a density estimate and provide a means of assessing the porosity remaining in the sample following compaction, we calculated the theoretical, zero-porosity densities from the mass and volume of the unit cell for the material in question at the measurement temperature and applied piston pressure (see Appendix A and the results in Table A1).

[16] Following the compaction phase of an experiment, we estimated the sample density from the initial sample mass and from the sample volume, which was given by the known diameter of the sample chamber and the sample length, l, measured as discussed above by the position of the compaction piston. These density estimates were in agreement with the zero-porosity density estimates, given in Table A1, suggesting the compaction method was successful [*Helgerud*, 2001]. For ice Ih, full compaction was verified by the optical clarity of the sample following the experiment (image given by *Helgerud* [2001, Figure 5.8]). In contrast, sI and sII hydrate samples retrieved by cooling the chamber with liquid nitrogen during depressurization were cracked, tended to fracture into disks, and could not be used to constrain the sample density estimates.

2.3. Sample Fabrication

[17] Triply distilled water, frozen to form gas-free ice crystals, then ground and sieved to obtain a 180–250 μm grain size range, provided the seed ice base for all samples described here. For each experiment, approximately 14 g of seed ice were loaded into the sample chamber, which was surrounded by a 0.1 mm thick Teflon liner. The pressure vessel assembly and sample loading were carried out in a chest freezer prior to suspending the vessel in the temperature-controlled liquid bath. The pore space was then evacuated via the gas line. Subsequent steps depended on the sample type, as described below.

2.3.1. Ice Ih

[18] Following evacuation of the pore space, the bath temperature was raised to −5°C in preparation for uniaxial compaction of the sample with the hydraulic piston. Preliminary testing demonstrated that a 43 MPa compaction pressure was sufficient to remove the sample porosity, and additional applied pressure extruded significant quantities of ice from between the pistons. For the two samples reported here, compaction shortened the samples from their initial lengths of 50.4 and 49.8 mm to 29.3 and 29.1 mm, respectively. Final sample length depended much more on initial sample mass (14.0 versus 13.9 g) than on compaction rate (6–8 μm s^{-1} versus 1.3 μm s^{-1}).

[19] The applied load was reduced following compaction, to 33 MPa for the first sample, and 31.4 MPa for the second. To determine the temperature dependence of elastic properties in ice Ih, both samples were taken through two temperature cycles, with wave speeds measured from −20 to −5°C in 5°C steps. To determine the pressure dependence of the elastic properties, the applied pressure was cycled at each temperature: between 22.5 and 33 MPa in the first sample, and between 20.9 and 31.4 MPa in 1.05 MPa steps in the second sample. Pressure and temperature cycling took 8–9 days, during which time the samples shortened an additional 0.2 mm as a result of ice extrusion from between the pistons.

2.3.2. The sI Methane Hydrate

[20] The two sI methane hydrate samples described here were synthesized directly in the wave speed measurement chamber using the methodology of *Stern et al.* [1998, 1996]. Following evacuation of the seed ice pore space, samples were connected via the gas line to a gas reservoir suspended in a temperature controlled bath with the sample vessel and pressurized with methane to ∼25 MPa. The bath temperature was then raised from −20 to +17°C over 8.5 h for the first sample and 11 h for the second. During this warming, gas pressure in the closed sample plus gas reservoir system rose to a peak of ∼33 MPa.

[21] As seed ice warmed in the presence of high-pressure methane, ice began converting to methane hydrate. In this synthesis method, as seed ice cores melt, the melt extrudes from the hydrate encasements, forming additional hydrate along grain boundaries and junctions in the initial seed ice pack [*Stern et al.*, 2004]. This highly reproducible formation technique produces porous methane hydrate samples with a bulk composition of $CH_4 \cdot nH_2O$, where $n = 5.89 \pm 0.01$ [*Stern et al.*, 2000]. This is equivalent to 97.6% cage occupancy ($\chi = 0.976$).

[22] Following hydrate synthesis, the system was cooled to −20°C, and pore pressure was reduced to 2 MPa to maintain sample stability while minimizing resistance to compaction. Computer controlled compaction began by advancing the compaction piston at an average rate of 1.2 μm s^{-1}, slightly lower than the 1.3 μm s^{-1} rate used for ice Ih. Unlike in ice Ih, initial compaction of sI (and sII) gas hydrate did not proceed continuously, and complete compaction required a peak axial pressure of 105 MPa, nearly 2.5 times that required for ice Ih. During the initial stages of hydrate compaction, pressure built up and was then released, causing the piston to move downward in a step-like fashion. These advances were often accompanied by an audible 'pop' emanating from the apparatus, presumably from breaking intergranular bonds. No equivalent behavior was observed in the ice samples. When the applied axial pressure reached 105 MPa, the Quizix pump was switched to constant pressure mode to maintain the 105 MPa pressure for 9 h at −20°C, then 15 h at 5°C, then 5 h at 15°C. The compaction process ended when the sample length stabilized at 15°C. To ensure methane hydrate stability near the gas line port during the compaction process, the gas line pressure was raised to 16 MPa prior to raising the temperature to 5°C. The temperature increase to 15°C further increased the gas pressure in the line to 22 MPa.

[23] To examine wave speed variations with temperature, temperature was cycled twice between −15 and 15°C, with measurements every 5°C. To ensure equivalent pressure conditions, the gas line pressure was adjusted to 25 MPa, and the piston pressure to 62 MPa at each temperature step. Once the wave speed was determined at a given temperature step, the piston pressure was cycled between 30.5 and 97.7 MPa to measure the wave speed dependence on axial pressure.

[24] After completing the temperature and pressure cycling, the applied axial pressure was lowered in 3.4 MPa steps, with approximately 1 h spent at each pressure. Gas line pressure was maintained at 25 MPa. Wave speed measurements ceased when the gas pressure broke the sample/acoustic endcap contact.

2.3.3. The sII Methane-Ethane Hydrate

[25] *Subramanian et al.* [2000] reported direct evidence that methane and ethane gas, both sI hydrate formers, formed sII hydrate for mixtures containing ∼75–99% methane. We formed sII methane-ethane hydrate from a source gas of 90.2% methane and 9.8% ethane, using the same pressures and temperatures described above for sI methane hydrate. Thermodynamic modeling showed ethane would not condense out of the source gas mixture over the pressure and temperature ranges utilized during the experiment (S. Subramanian, personal communication, 2000). A sample made from deuterated ice with this source gas was determined to be sII hydrate using neutron powder diffraction [*Rawn et al.*, 2002].

[26] To estimate cage occupancy, a portion of the sample was dissociated into a known volume using the apparatus described by *Kvenvolden et al.* [1984], and the evolved gas was analyzed with a gas chromatograph. The cage occupancy was determined to be 94%, with a gas composition of 79.25% methane, 20.75% ethane.

[27] Sample compaction was accomplished as described for sI methane hydrate, though with longer hold times at peak compaction pressure. Initial compaction was performed at −20°C with gas pressures ranging from 2 to 2.5 MPa. As with sI gas hydrate, we observed a stepwise compaction with audible "pops" over the first several millimeters of compaction. The maximum allowed piston pressure of 105 MPa was held for 2 days at −20°C. At 5°C, with 18 MPa gas pressure, the 105 MPa load was held for 4 days, with an additional 24 h at 15°C and 20 MPa gas pressure.

[28] We examined temperature variations of wave speed with measurements made every 5°C in two temperature cycles between −20 and 10°C. As with sI methane hydrate, we used an applied piston pressure of 61 MPa. Unlike the sI experiment, however, gas line pressure was allowed to vary freely with temperature, ranging from 14.75 to 19.95 MPa. No net change in pressure was observed from one temperature cycle to the next. Once the wave speed was determined at a given temperature step, piston pressure was cycled between 30.5 and 91.6 MPa to measure the wave speed dependence on pressure.

[29] To examine the wave speed response to applied pressures smaller than the gas pressure, the sample was allowed to equilibrate to a low-stress state relative to the conditions during pressure cycling. For 25 h, the sample was held at −20°C and 6.3 MPa applied load, and 2.6 MPa gas pressure. Piston pressure was then further reduced to 3.05 MPa at 0.03 MPa h^{-1}, held for 23 h, then reduced by 0.03 MPa h^{-1} to 0.8 MPa. After 8.5 h, piston pressure was reduced at 0.03 MPa h^{-1} to 0 MPa and held for 10 h prior to sample tear down. Internal friction within the apparatus kept the piston from being pushed off the sample. The wave speed response in both sI and sII hydrate was similar, but slowly reducing the applied pressure in the sII experiment allowed the piston to remain in contact with the sample for the entire decompression.

3. Results and Discussion

[30] Our experimental program yielded two types of results: (1) From temperature and pressure cycles we obtain linear wave speed dependencies with which to calculate Poisson's ratio as well as bulk, compressional and shear moduli for ice Ih, sI methane hydrate, and sII methane-ethane hydrate. (2) During initial compaction and final unloading for both hydrate types, we observed wave speed increases resulting from rapid annealing of grains and crack healing.

3.1. Temperature and Pressure Cycling Results

[31] Figures 2 and 3 illustrate the linear dependence of wave speed on temperature and pressure for ice Ih, sI methane hydrate and sII methane-ethane hydrate. Two temperature

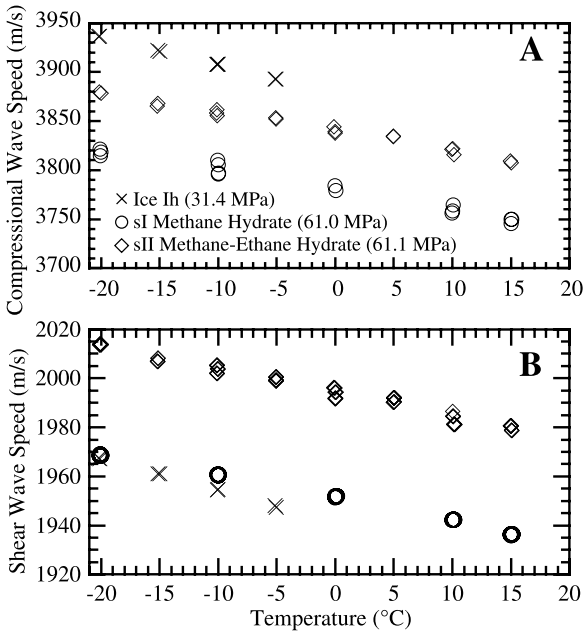

Figure 2. (a) Compressional and (b) shear wave speed dependence on temperature for ice Ih, sI methane hydrate, and sII methane-ethane hydrate. Piston pressure is given in parentheses. Two temperature cycles are plotted for each material, demonstrating the consistent, elastic nature of the system. Increased scatter in the compressional wave speed results is due to using the precursor P wave from the shear crystal, which is smaller and less clearly defined than the shear wave. For clarity, therefore, only every 10th point is shown for methane hydrate, and every 20th point is shown for methane-ethane hydrate in Figure 2a.

cycles are shown for each material in Figure 2. Consistency between cycles indicates a consistent and elastic response for all three materials to the temperature cycling. The decreasing shear wave speed with increasing pressure shown in Figure 3b is unusual but has been observed in amorphous glasses [*Xu*, 1996] and has been seen previously in ice Ih [*Gagnon et al.*, 1988; *Shaw*, 1986].

3.1.1. Ice Ih

[32] To test our measurement technique and to provide a context for assessing our gas hydrate measurements, we compared our pressure and temperature dependence of wave speeds in ice Ih to published results. Results from 2-D planar regressions to the wave speeds (Table 1) are within the published range of wave speeds for polycrystalline ice Ih and aggregate averages from single-crystal measurements [*Gagnon et al.*, 1988; *Gammon et al.*, 1983; *Gold*, 1958; *Northwood*, 1947; *Shaw*, 1986; *Smith and Kishoni*, 1986]. The previously published work is compiled by *Helgerud* [2001].

3.1.2. The sI Methane Hydrate

[33] Over our measurement range of −20 to 15°C and 30.5–97.7 MPa applied pressure, compressional and shear wave speeds are linearly dependent on temperature and applied pressure (Figures 2 and 3). Fits to the wave speed data and calculated fits for Poisson's ratio, compressional, shear and bulk moduli are given in Table 2. As with ice Ih and sII methane-ethane hydrate, shear wave speed decreases with increasing pressure. The pressure dependence of density is sufficiently different between ice Ih and hydrate, however, to produce a decrease in calculated shear modulus (equation (5)) with increasing pressure for ice Ih, compared to an increase for both hydrate structures.

[34] The few published wave speed estimates in methane hydrate are measured using Brillouin scattering [*Baumert et al.*, 2003; *Kiefte et al.*, 1985; *Shimizu et al.*, 2002; *Whiffen et al.*, 1982]. These single-crystal measurements produce wave speed information along each crystal axis. Obtaining average values appropriate for randomly oriented collections of hydrate crystals requires combining results from the different crystal axes. This averaging is not consistent from study to study however, and some studies do not discuss the averaging process.

[35] *Kiefte et al.* [1985], analyzing data first published by *Whiffen et al.* [1982], report a compressional wave speed of 3370 m s^{-1} for methane hydrate at −10°C and 5 MPa. From Table 2, our prediction for their experimental condition is 3786 m s^{-1}, more than 10% higher than the *Kiefte et al.* [1985] result. This discrepancy is likely due to the quality of the methane hydrate sample used in the Brillouin scattering experiments, however. *Kiefte et al.* [1985] and *Whiffen et al.* [1982] reported methane hydrate to be "the most difficult hydrate to produce." They were only able to obtain two Brillouin scattering spectra, and the sample was "cloudy and of poor quality."

[36] The considerable technical difficulties faced by *Whiffen et al.* [1982] were surmounted by *Shimizu et al.* [2002] and *Baumert et al.* [2003]. We use the approach of *Zha et al.* [2000] to convert the axis-dependent moduli results

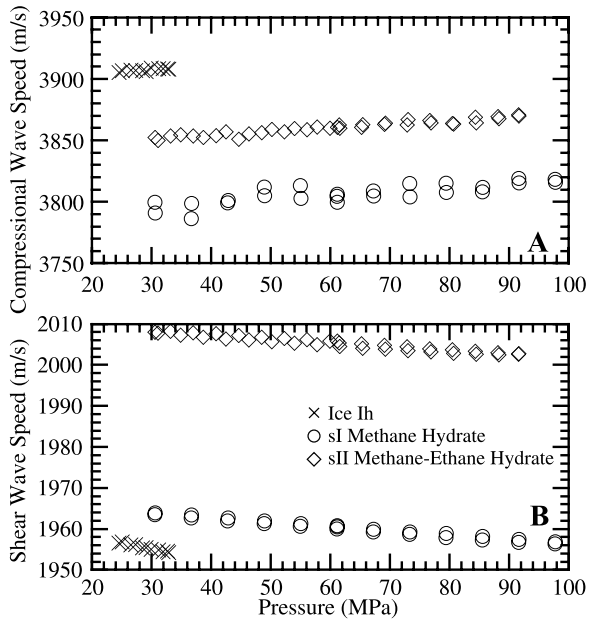

Figure 3. (a) Compressional and (b) shear wave speed dependence on piston pressure at −10°C in ice Ih, sI methane hydrate, and sII methane-ethane hydrate. Decreasing shear wave speed with increasing pressure, though unusual, has previously been observed in ice Ih [*Gagnon et al.*, 1988; *Shaw*, 1986] and amorphous glasses [*Xu*, 1996]. For clarity, only every second point is shown for ice Ih, and every fifth point is shown for methane-ethane hydrate.

Table 1. Regressions of V_p and V_s, ν, and M, G, and K Versus Temperature and Piston Pressure for Compacted, Polycrystalline Ice Ih[a]

	F(T,P) = $aT + bP + c$*			
	a[b]	b[b]	c[b]	Uncertainty[c]
V_p (m s^{-1})	−2.67 ± 0.05	0.2 ± 0.08	3864 ± 2	±1.5
V_s (m s^{-1})	−1.244 ± 0.005	−0.198 ± 0.007	1942.4 ± 0.2	±1.5
ν	$-(2.0 \pm 0.6) \times 10^{-5}$	$(6.8 \pm 0.9) \times 10^{-5}$	0.3310 ± 0.0002	±3
M (GPa)	$-(2.15 \pm 0.04) \times 10^{-2}$	$(4.02 \pm 0.03) \times 10^{-3}$	13.69 ± 0.02	±4
G (GPa)	$-(5.03 \pm 0.02) \times 10^{-3}$	$-(3.0 \pm 0.2) \times 10^{-4}$	3.459 ± 0.0007	±4
K (GPa)	$-(1.48 \pm 0.04) \times 10^{-2}$	$(3.4 \pm 0.5) \times 10^{-3}$	9.07 ± 0.02	±6

[a]V_p, compressional wave speeds; V_s, shear wave speeds; ν, Poisson's ratio; M, dynamic compressional wave; G, shear moduli; and K, bulk moduli; temperature of −20 to −5°C; and piston pressure of 22.4 to 32.8 MPa. Calculated density range was 0.920 to 0.923 g cm^{-3}.
[b]Units for a are the units of the property being fit divided by °C. Units for b are those of the property being fit divided by MPa. Units for c are those of the property being fit.
[c]Uncertainty is given as a percentage of the property being fit.

from *Shimizu et al.* [2002] and *Baumert et al.* [2003] (H. Shimizu, personal communication, 2006) to wave speeds. We compare their results with our predictions, which we extrapolate to their measurement conditions of 23°C and 18 to 580 MPa (Figure 4).

[37] Close agreement for compressional wave speeds, within 1% for low-pressure results from two very different hydrate formation and wave speed measurement techniques, is an encouraging validation of both methodologies. The 1–4% discrepancy in the low-pressure shear wave speed data is due in part to using the Voigt-Reuss-Hill average for obtaining bulk shear moduli from single-crystal results [*Zha et al.*, 2000]. Other averaging schemes from which shear wave speeds are calculated provide slightly different results.

[38] Despite very different sample fabrication and measurement techniques, our extrapolated results for bulk, polycrystalline sI methane hydrate are within 4.5%, and generally within 2%, of the single-crystal measurement results. This agreement indicates the utility of our fit parameters above our measured temperature and pressure ranges. Extrapolations below our measured pressure range are discussed in section 3.1.3.

3.1.3. The sII Methane-Ethane Hydrate

[39] As with ice and sI methane hydrate, wave speeds in sII methane-ethane hydrate are highly repeatable, and linear with temperature (Figure 2) and applied pressure (Figure 3). Fits to the wave speed data and the calculated fits for Poisson's ratio, compressional, shear and bulk moduli are given in Table 3.

[40] Published wave speed results are rare for sII hydrates, found naturally in systems formed from thermogenic gas containing ethane, propane and higher hydrocarbons. Such systems are abundant in the Gulf of Mexico [*Sassen et al.*, 2000], observed in Barkley Canyon, offshore Vancouver [*Lu et al.*, 2007], and have been inferred in other locations around the world [*Milkov*, 2005].

[41] *Kiefte et al.* [1985] used Brillouin spectroscopy to measure P wave speeds in several sII hydrates. At 0°C and 0.4 MPa, *Kiefte et al.* [1985] report a P wave speed through propane hydrate of 3691 m s^{-1}. From Table 3, our P wave speed prediction for methane-ethane hydrate for those conditions is 3821 m s^{-1}, 3.4% above the *Kiefte et al.* [1985] results. The difference can be explained using a key result from the *Kiefte et al.* [1985] work in which they note a nearly linear dependence of wave speed on the square root of the molecular weight of the cage occupant. From three different hydrates measured by *Kiefte et al.* [1985] at 0°C, the dependence of V_p on guest molecular weight, m_{guest}, can be written as

$$V_p = 4019 - 46.59\sqrt{m_{\text{guest}}}, \tag{6}$$

where V_p is in units of m s^{-1} and m_{guest} is in units of g mol^{-1}. Given our sample composition of 79.25% methane, 20.75% ethane, the average guest mass is 18.9 g mol^{-1}. From equation (6), the predicted V_p is 3817 m s^{-1}, in excellent agreement with Table 3 based prediction of 3821 m s^{-1} at 0°C and 0.4 MPa.

[42] Agreement with the low-pressure work of *Kiefte et al.* [1985] for sII hydrate suggests that the planar fits provided in Tables 1–3 are valid below our measurement ranges. As a check on the validity of extrapolating our linear fits beyond the stated measurement ranges, we continued measuring S wave speeds during sample decompression

Table 2. Regressions of V_p and V_s, ν, and M, G, and K Versus Temperature and Piston Pressure for Compacted, sI Methane Hydrate[a]

	F(T,P) = $aT + bP + c$*			
	a[b]	b[b]	c[b]	Uncertainty[c]
V_p (m s^{-1})	−1.84 ± 0.03	0.31 ± 0.02	3766 ± 2	±1.5
V_s (m s^{-1})	−0.892 ± 0.005	−0.100 ± 0.003	1957.0 ± 0.2	±1.5
ν	$-(9 \pm 4) \times 10^{-5}$	$(6.6 \pm 0.3) \times 10^{-5}$	0.3151 ± 0.0002	±3
M (GPa)	$-(1.64 \pm 0.02) \times 10^{-2}$	$(4.02 \pm 0.03) \times 10^{-3}$	13.11 ± 0.01	±4
G (GPa)	$-(4.2 \pm 0.02) \times 10^{-3}$	$(9 \pm 1) \times 10^{-5}$	3.541 ± 0.0008	±4
K (GPa)	$-(1.09 \pm 0.02) \times 10^{-2}$	$(3.8 \pm 0.2) \times 10^{-3}$	8.39 ± 0.01	±6

[a]Same as Table 1 except piston pressure of 30.5 to 97.7 MPa. Calculated density range was 0.924 to 0.933 g cm^{-3}.
[b]Units for a are the units of the property being fit divided by °C. Units for b are those of the property being fit divided by MPa. Units for c are those of the property being fit.
[c]Uncertainty is given as a percentage of the property being fit.

*Table heading is corrected here. The article as originally published is online.

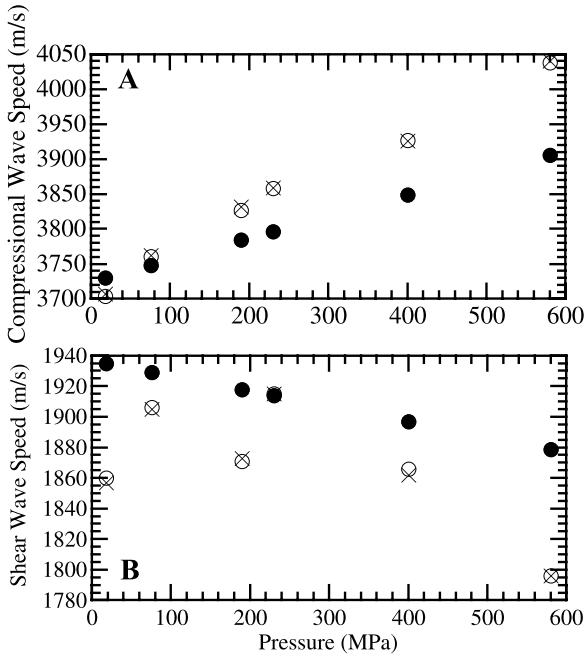

Figure 4. (a) Compressional and (b) shear wave speed dependence on pressure in sI methane hydrate. Solid circles are extrapolations from our linear fits to the pressures used in the single-crystal Brillouin scattering experiments of *Shimizu et al.* [2002] (open circles) and *Baumert et al.* [2003] (crosses). Our predictions are extrapolated to their measurement temperature of 23°C. Despite very different sample fabrication and measurement techniques, our extrapolated results for bulk, polycrystalline sI methane hydrate differ from the single-crystal results at most by 4.5% and generally by less than 2%.

prior to sample tear down. At −20°C and 3.05 MPa, just prior to the onset of sample cracking (discussed in section 3.2), the measured S wave speed of 2020.5 m s^{-1} is in excellent agreement with the Table 3 fit prediction of 2018.8 m s^{-1}. P waves, being much smaller in amplitude than the S waves, are not observable at such low applied pressures, but the agreement discussed above with V_p predictions from *Kiefte et al.* [1985] suggests our P wave fits are also valid to low pressures.

3.2. Inelastic Hydrate Response to Applied Pressure Changes

[43] During experimental periods when the hydrate sample is not fully compacted, such as during the compaction process, or during final decompression when the sample begins to crack, we see evidence of intergranular bonding affecting our macroscopic wave speed results. These changes are observable in ice Ih, sI methane hydrate [*Helgerud*, 2001] and sII methane-ethane hydrate over timescales as short as 30 min. These annealing processes have implications for mechanical measurements made on disturbed material, such as recovered hydrate-bearing core.

3.2.1. Annealing During Compaction

[44] In our early experiments utilizing a manual hydraulic pump to compact sI methane hydrate samples, active maintenance of the pump pressure was paused overnight. Because the piston was free to move, the sample continued to compact slightly, and the applied pressure from the manual pump relaxed during this pause. As shown in Figure 5, the wave speed increase during the pause in active pressure maintenance was more rapid than the increase observed while the piston pressure was being actively maintained at the 105 MPa compaction pressure. Once the piston pressure was manually restored and held at 105 MPa, the wave speed initially fell, then began increasing again along the active compaction trend line established prior to the overnight pause in active compaction.

[45] We attribute this behavior to annealing at grain contacts. Our initially porous, granular samples were compacted to remove pore space between grains. During the pause in active compaction, intergranular contacts annealed, cementing grains. This cementing process stiffened the sample, increasing the wave speed above and beyond the increase expected from porosity reduction. When active compaction resumed, these grain-to-grain contacts were broken, returning the sample to a collection of uncemented grains in contact. After the intergranular bonds were broken, the wave speed increase again followed the trend due to porosity reduction during compaction. We observed this effect in ice Ih as well as in both hydrate structures, though the process occurred more quickly in ice Ih than in gas hydrate. This is consistent with the higher mobility of water in the ice Ih crystal lattice compared to sI or sII gas hydrate [*Sloan and Koh*, 2007, Table 2.8].

Table 3. Regressions of V_p and V_s, ν, and M, G, and K Versus Temperature and Piston Pressure for Compacted, Polycrystalline sII Methane-Ethane Hydrate[a]

	F(T,P) = $aT + bP + c$*			
	a[b]	b[b]	c[b]	Uncertainty[c]
V_p (m s^{-1})	−1.825 ± 0.008	(3.10 ± 0.05) × 10^{-1}	3821.8 ± 0.3	1.5
V_s (m s^{-1})	−0.894 ± 0.002	−(0.87 ± 0.01) × 10^{-1}	2001.14 ± 0.08	1.5
ν	−(1.4 ± 0.1) × 10^{-5}	(6.29 ± 0.07) × 10^{-5}	0.31119 ± 0.00004	3
M (GPa)	−(1.564 ± 0.005) × 10^{-2}	(4.02 ± 0.03) × 10^{-3}	13.407 ± 0.002	4
G (GPa)	−(4.021 ± 0.007) × 10^{-3}	(1.66 ± 0.04) × 10^{-4}	3.6764 ± 0.0003	4
K (GPa)	−(1.028 ± 0.005) × 10^{-2}	(3.80 ± 0.03) × 10^{-3}	8.505 ± 0.002	6

[a]Same as Table 1 except temperature of −20 to 10°C and piston pressure of 30.5 to 91.6 MPa. Sample density calculated theoretically as a function of temperature and pressure with 94% cage occupancy, 79.25% methane, 20.75% ethane. Calculated density range was 0.917 to 0.931 g cm^{-3}.

[b]Units for a are the units of the property being fit divided by °C. Units for b are those of the property being fit divided by MPa. Units for c are those of the property being fit.

[c]Uncertainty is given as a percentage of the property being fit.

*Table heading is corrected here. The article as originally published is online.

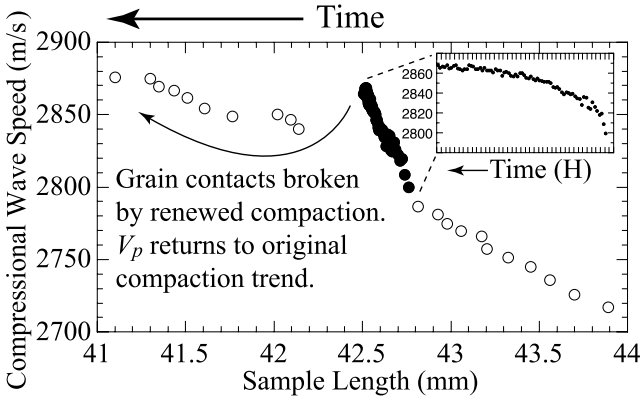

Figure 5. Compressional wave speed, V_p, during compaction of sI methane hydrate. V_p increases as porosity is reduced, and the sample shortens during active compaction (open circles). An additional V_p increase occurs during a break in compaction as mobile molecules cement hydrate grains together (solid circles). This effect is observable within 30 min, the time separation between data points (inset shows V_p dependence on time). Renewing active compaction breaks the intergranular bonds, returning V_p to the preexisting, porosity-controlled trend.

3.2.2. Annealing During Decompression

[46] Prior to completing a wave speed experiment, the applied piston pressure was reduced to zero. Both hydrate types responded elastically, with the wave speed closely following predictions made using the fits in Tables 2 and 3 until the applied load dropped below the gas pressure used to stabilize the hydrate (Figure 6). Once the gas pressure exceeded the piston pressure, gas invaded and expanded cracks that formed during decompression. On the basis of step increases in the measured sample length during decompression, the maximum crack aperture was no wider than 0.5 μm, with most cracks being narrower. Crack formation abruptly reduced the measured wave speed, which was then observed to recover to within 99.9% of its precrack value within approximately 30 min (Figure 6).

[47] Because the decompression shown in Figure 6 was accomplished at 15°C, the observed crack healing was not due to the formation of ice. We instead attribute the wave speed recovery to gas hydrate annealing, which partly restored the cemented grain-to-grain contacts that existed prior to cracking. As shown in Figure 6, each successive piston pressure reduction allowed more and perhaps larger cracks to form, further reducing the measured wave speed, but crack healing became noticeable when piston pressure was held constant after each pressure reduction. We observed this effect in both hydrate structures with the same time dependence, but because the ice Ih experiment was done under vacuum rather than with excess gas pressure, cracks did not open up in ice Ih during decompression and there was no opportunity to observe crack healing.

[48] Evidence of hydrate annealing on the time and length scales discussed here can also be seen in SEM micrographs taken at different stages of hydrate formation from ice, the formation technique used in our study. *Stern et al.* [2004] showed how hydrate initially dotted with mesopores on the order of tenths of a micron across transforms to fully dense hydrate in less than 70 min (L. A. Stern, personal communication, 2005).

3.2.3. Field Implications of Annealing

[49] The crack-healing behavior of gas hydrate can also be observed in hydrate-bearing core samples recovered in the field. When hydrate-bearing core is recovered using conventional coring techniques, the core depressurizes as it transits up to the recovery system. When stored in pressure vessels for further study, these cores are often repressurized with methane gas. The same depressurization/repressurization cycle occurs over a shorter time span when pressure cores, maintained at their in situ hydrostatic pressure, are transferred to a laboratory instrument or storage chamber at atmospheric pressure. In both cases, however, not only is methane introduced as a free gas during repressurization, but methane can also come out of solution as pore water in the core depressurizes. These repressurized samples can undergo hydrate recrystallization, causing the wave speed to recover, or even exceed its predisturbance value [*Waite et al.*, 2008].

[50] The extent of wave speed recovery depends strongly on the extent of hydrate dissociation during recovery, however, and should not be relied upon as a process capable of producing in situ wave speeds in recovered core [*Waite et al.*, 2008]. For mechanical property measurements, this underscores the need for pressurized core recovery, and physical property measurements made without depressurizing the core, using systems such as described by *Yun et al.* [2006].

4. Conclusions

[51] On the basis of simultaneous P and S wave speed measurements and calculations of sample density for ice Ih, sI methane hydrate and sII methane-ethane hydrate, we derive pressure and temperature dependencies of a suite of elastic properties for all three materials. We observe several similarities between ice Ih and gas hydrate: (1) Wave speeds

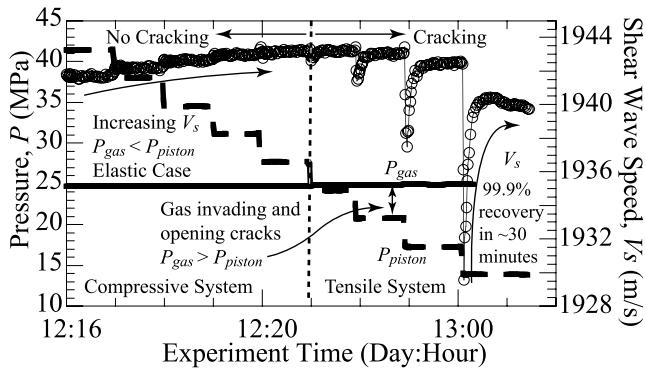

Figure 6. Shear wave speed, V_s, during final piston decompression in sI methane hydrate at 15°C. While piston pressure (P_{piston}, thick dotted line) exceeds the gas pressure (P_{gas}, thick solid line), V_s (open circles) increases as in Figure 3. When P_{piston} drops below P_{gas}, gas invades and opens cracks, causing V_s to drop. Molecular migration forms hydrate bridges across newly opened cracks, restoring V_s to 99.9% of its precrack value within 30–35 min.

differ by less than 3% between materials, and (2) shear wave speed decreases with increasing axial pressure.

[52] Despite these similarities, significant property differences between ice and hydrate exist, indicating that ice Ih cannot always be considered a direct analog for gas hydrate: (1) Relative to ice Ih, sI and sII hydrate have a dramatically larger resistance to uniaxial compaction, and (2) the shear modulus of ice Ih decreases with increasing axial pressure, whereas the shear modulus in sI and sII gas hydrate increases with increasing axial pressure.

[53] There are also wave speed differences between the two hydrate structures that are well above our sample-to-sample wave speed variability. Even for a given hydrate structure, *Kiefte et al.* [1985] show that wave speed varies as a function of the guest molecule type. The proposed square root dependency of wave speed on guest molecule mass suggested by *Kiefte et al.* [1985] is a promising theoretical approach, but precise quantification of physical properties will likely require direct testing of each specific gas hydrate.

[54] The ability of these crystalline materials to anneal, healing cracks over a tenth of a μm length scale and $\sim$30 min time scale has implications for studying macroscopic physical properties of hydrate bearing sediment. Recovered hydrate-bearing core will likely be affected measurably by annealing, crack healing, and the resulting partial restoration of the in situ sample stiffness. Because the extent of this restoration relative to the extent of sample disruption during recovery is not known, this crack healing phenomena cannot be assumed to fully return the acoustic properties of extracted cores to their in situ values.

Appendix A

[55] Sample density is required to calculate the elastic moduli given in equations (3)–(5). We calculate densities from the mass and volume of the unit cell for the material in question at the measurement temperature and applied piston pressure.

A1. Unit Cell Mass

[56] Unit cell masses, m_{cell}, are calculated by summing the atomic masses of the individual components, m_i, in each crystallographic unit cell. In general,

$$m_{\text{cell}} = n_{\text{H}_2\text{O}} m_{\text{H}_2\text{O}} + n_{\text{cage}} \chi_{\text{cage}} \sum_i f_i m_i \qquad \text{(A1)}$$

where n_{H2O} is the number of water molecules, each with mass $m_{\text{H2O}} = 2.9915 \times 10^{-26}$ kg; n_{cage} is the number of cages available for hydrate-forming molecules; χ_{cage} is the fraction of occupied cages, taken to be 0.94 ± 0.04 for both hydrate structures based on dissociation tests during this study; and f_i is the fraction of cage occupants of mass m_i. In our methane-ethane hydrate, we estimate $f_{\text{CH4}} = 0.8$ and $f_{\text{C2H6}} = 0.2$ from chromatography tests of dissociated material.

[57] In ice Ih, for which $n_{\text{H2O}} = 4$ and $n_{\text{cage}} = 0$ [*Sloan and Koh*, 2007], the unit cell mass is $m_{\text{ice Ih}} = 1.5966 \times 10^{-25}$ kg. In sI methane hydrate, for which $n_{\text{H2O}} = 46$, $n_{\text{cage}} = 8$ [*Sloan and Koh*, 2007], $f_{\text{CH4}} = 1$, and $m_{\text{CH4}} = 2.6649 \times 10^{-26}$ kg, the unit cell mass is $m_{\text{CH4Hydrate}} = 1.5765 \times 10^{-24}$ kg. For sII methane/ethane hydrate, for which $n_{\text{H2O}} = 136$, $n_{\text{cage}} = 24$ [*Sloan and Koh*, 2007], $f_{\text{CH4}} = 0.8$, $m_{\text{CH4}} = 2.6649 \times 10^{-26}$ kg, $f_{\text{C2H6}} = 0.2$, and $m_{\text{C2H6}} = 4.9950 \times 10^{-26}$ kg, the unit cell mass is $m_{\text{CH4-C2H6Hydrate}} = 4.7748 \times 10^{-24}$ kg.

A2. Unit Cell Volume

[58] We assume the unit cell volume, $V(T,P)$, is a function of temperature, T, and applied pressure, P. Any dependence on cage occupant is neglected. In response to pressure or temperature changes, the fractional unit cell volume change is given by

$$\frac{dV}{V} = \frac{1}{V}\left(\frac{\partial V}{\partial T}\right)_P dT + \frac{1}{V}\left(\frac{\partial V}{\partial P}\right)_T dP = \alpha dT + \kappa_T dP, \qquad \text{(A2)}$$

where α is the thermal expansivity and κ_T is the isothermal compressibility.

[59] In general, α and κ_T depend on both temperature and pressure. However, we assume here that both are constants. Integrating (A2) from initial conditions V_0 at T_0 and P_0 to final conditions V at T and P and rearranging terms, we get an approximate equation of state for an isotropic solid with constant thermal expansivity and isothermal compressibility,

$$V \approx V_0 e^{\alpha(T-T_0)} e^{-\kappa_T(P-P_0)}. \qquad \text{(A3)}$$

Published unit cell volumes of ice Ih, sI methane hydrate and sII THF hydrate are available over a range of temperatures at 1 atm pressure. We can therefore estimate the unit cell volumes of ice Ih, sI and sII gas hydrate over a range of temperatures and pressures if we can estimate their respective isothermal compressibilities using the relationship

$$V = V(T, P_0) e^{-\kappa_T(P-P_0)}, \qquad \text{(A4)}$$

where $V(T, P_0)$ comes from the published unit cell volume measurements at $P_0 = 1$ atm $= 0.1$ MPa.

[60] For ice Ih, the unit cell volume and its variation with temperature from 10 to 265 K at constant pressure of 1atm, are taken from measurements by *Röttger et al.* [1994] with corrections to the fitting coefficients supplied by W. F. Kuhs (personal communication, 1999) [*Helgerud*, 2001]. For sI methane hydrate, which has a cubic structure, V_0 is taken as the cube of the lattice parameter a_I, measured as a function of temperature from 80 to 210 K at 1 atm by *Shpakov et al.* [1998]. For sII methane-ethane hydrate, the lattice parameter a_{II}, is taken from measurements by *Tse* [1987] on sII THF hydrate from 20 to 250 K at 1 atm.

[61] We estimate the isothermal compressibility, κ_T, for ice Ih as 0.115 GPa^{-1}, consistent with available published data [*Gow and Williamson*, 1972; *Richards and Speyers*, 1914] for the temperature range used in our experiments. For sI methane and sII methane-ethane hydrate, κ_T is estimated from κ_T in ice Ih and thermodynamic first principles, as first proposed by *Whalley* [1980] and described in detail by *Helgerud* [2001, Chapter 2]. Using this method, the ratios between the isothermal compressibility of ice and sI and sII gas hydrates are calculated to be 0.906 and 0.874, respectively [*Helgerud*, 2001]. Therefore, the estimate for the isothermal compressibility of sI methane

Table A1. Regressions of Density Versus Temperature for Solid Ice Ih, sI Methane Hydrate, and sII Methane-Ethane Hydrate[a]

Material	$\rho(T,P) = aT + bP + c$*			
	a[b]	b[b]	c[b]	Uncertainty[c]
Ice Ih	-1.5035×10^{-4}	1.0594×10^{-4}	0.91673	3
sI methane hydrate	-2.3815×10^{-4}	1.1843×10^{-4}	0.92435	3
sII methane-ethane hydrate	-1.7719×10^{-4}	1.2228×10^{-4}	0.91801	3

[a]Both hydrate structures are assumed to have 94% cage occupancy. The ratio of methane to ethane in the sII hydrate is assumed to be 4:1. Temperature and pressure ranges are given in Tables 1–3.
[b]Units for a are the units of the property being fit divided by °C. Units for b are those of the property being fit divided by MPa. Units for c are those of the property being fit.
[c]Uncertainty is given as a percentage of the property being fit.

hydrate is 0.127 GPa^{-1} and for sII methane-ethane hydrate is 0.132 GPa^{-1}.

[62] Applying these results to the measurement conditions used in our experiments and assuming the applied, uniaxial piston pressure approximates the hydrostatic pressure, P, we obtain density models that are nearly linear in temperature and pressure and are well approximated by 2-D planar regression. The planar fit equations are given in Table A1.

A3. Density Uncertainty Estimate

[63] Uncertainties in V, κ_T, and cage occupancy lead to an uncertainty of a few percent in our density estimates given in Table A1. As shown below, a systematic density overestimate of ~1% occurs by assuming that the measured uniaxial piston pressure P_p approximates the hydrostatic pressure P.

[64] Ignoring friction between the sample and sidewall, and assuming the lateral strain is zero, the lateral pressure in the sample, P_l, is [*Kirby*, 1999]

$$P_l = \left(\frac{v}{1-v}\right)P_p, \tag{A5}$$

where ν is Poisson's Ratio (see Tables 1–3). The mean pressure, P_m, is:

$$P_m = \frac{1}{3}\left(P_p + 2P_l\right). \tag{A6}$$

For the peak uniaxial pressure of 105 MPa, substituting the mean pressure in equations (A3) and (A4) for the hydrostatic pressure leads to a volume that is 0.5% larger that that obtained by assuming the uniaxial pressure is equivalent to the hydrostatic pressure.

[65] The actual systematic volume error is slightly more than 0.5% because, though (A6) requires zero lateral strain in the sample, there could be up to 0.4% lateral strain if the 0.1 mm thick Teflon chamber liner compressed to zero thickness. The lateral and mean pressures are therefore slightly less than that predicted from (A5) and (A6), with a correspondingly slight increase in the volume calculated from (A3) and (A4). The difference in volume estimated using the hydrostatic versus uniaxial pressure is not expected to exceed 1%, and since it is the uniaxial piston pressure that we control and measure, we choose to use it throughout our analysis. Given the uncertainties discussed above, we conservatively estimate an uncertainty of 3% for our density fits listed in Table A1.

*Table heading is corrected here. The article as originally published is online.

[66] **Acknowledgments.** This work was supported by NSF grant OCE-97-10506, DOE grants DE-FG0386ER 13601 and DE-FG07-96ER 14723, DOE/LLNL contract W-7405-ENG-48, GRI grant 5094-210-3235-1, NEDO, as well as by the U.S. Geological Survey's Coastal and Marine Geology and Eastern Region Gas Hydrate Programs. Tom Lorenson performed the gas chromatography work, and Susan Circone performed the precision dissociation work. Laura Stern helped with the hydrate synthesis, and Shiva Subramanian helped with the gas properties. This manuscript benefited from the reviews of David Cole and William Winters, and discussions with Brandon Dugan, Jack Germaine, and Carlos Santamarina. Any use of trade names is for descriptive purposes only and does not imply endorsement by the U.S. Government.

References

Archer, D. (2007), Methane hydrate stability and anthropogenic climate change, *Biogeosciences*, *4*, 521–544.

Baumert, J., C. Gutt, W. Press, J. S. Tse, and S. Janssen (2002), Low frequency dynamics of gas hydrates studied with inelastic incoherent neutron scattering, paper presented at the 4th International Conference on Gas Hydrates, Heat Transfer Soc. of Jpn., Yokohama, 19–23 May.

Baumert, J., C. Gutt, V. P. Shpakov, J. S. Tse, M. Krisch, M. Muller, H. Requardt, D. D. Klug, S. Janssen, and W. Press (2003), Lattice dynamics of methane and xenon hydrate: Observation of symmetry-avoided crossing by experiment and theory, *Phys. Rev. B*, *68*, 174301.

Chand, S., and T. A. Minshull (2003), Seismic constraints on the effects of gas hydrate on sediment physical properties and fluid flow: A review, *Geofluids*, *3*, 275–289, doi:10.1046/j.1468-8123.2003.00067.x.

Chand, S., T. A. Minshull, J. A. Priest, A. I. Best, C. R. Clayton, and W. F. Waite (2006), An effective medium inversion algorithm for gas hydrate quantification and its application to laboratory and borehole measurements of gas hydrate-bearing sediments, *Geophys. J. Int.*, *166*, 543–552, doi:10.1111/j.1365-246X.2006.03038.x.

Collett, T. S. (2002), Energy resource potential of natural gas hydrates, *AAPG Bull.*, *86*, 1971–1992.

Dallimore, S. R., and T. S. Collett (2005), Summary and implications of the Mallik 2002 gas hydrate production research well program, in *Scientific Results From the Mallik 2002 Gas Hydrate Production Well Program*, edited by S. R. Dallimore and T. S. Collett, *Geol. Surv. Can. Bull.*, *585*, 1–36.

Dickens, G. R., J. R. O'Neil, D. K. Rea, and R. M. Owen (1995), Dissociation of oceanic methane hydrates as a cause of the carbon isotope excursion at the end of the Paleocene, *Paleoceanography*, *10*(6), 965–972, doi:10.1029/95PA02087.

Gagnon, R. E., H. Kiefte, M. J. Clouter, and E. Whalley (1988), Pressure dependence of the elastic constants of ice Ih to 2.8 kbar by Brillouin spectroscopy, *J. Chem. Phys.*, *89*, 4522–4528, doi:10.1063/1.454792.

Gammon, P. H., H. Kiefte, and M. J. Clouter (1983), Elastic constants of ice samples by Brillouin sectroscopy, *J. Phys. Chem.*, *87*(21), 4025–4029, doi:10.1021/j100244a004.

Gold, L. W. (1958), Some observations on the dependence of strain on stress for ice, *Can. J. Phys.*, *36*, 1265–1275.

Gow, A. J., and T. C. Williamson (1972), Linear compressibility of ice, *J. Geophys. Res.*, *77*, 6348–6352, doi:10.1029/JB077i032p06348.

Helgerud, M. B. (2001), Wave speeds in gas hydrate and sediments containing gas hydrate: A laboratory and modeling study, Doctoral thesis, 251 pp., Stanford Univ., Palo Alto, Calif.

Helgerud, M. B., J. Dvorkin, A. Nur, A. Sakai, and T. Collett (1999), Elastic-wave velocity in marine sediments with gas hydrates: Effective medium modeling, *Geophys. Res. Lett.*, *26*, 2021–2024, doi:10.1029/1999GL900421.

Helgerud, M. B., W. F. Waite, S. H. Kirby, and A. Nur (2003a), Measured temperature and pressure dependence of compressional (V_p) and shear

(V_s) wave speeds in compacted, polycrystalline ice Ih, *Can. J. Phys.*, *81*, 81–87, doi:10.1139/p03-008.

Helgerud, M. B., W. F. Waite, S. H. Kirby, and A. Nur (2003b), Measured temperature and pressure dependence of V_p and V_s in compacted, polycrystalline sI methane and sII methane-ethane hydrate, *Can. J. Phys.*, *81*, 47–53, doi:10.1139/p03-016.

Holder, G. D., V. A. Kamath, and S. P. Godbole (1984), The potential of natural gas hydrates as an energy resource, *Annu. Rev. Energy*, *9*, 427–445, doi:10.1146/annurev.eg.09.110184.002235.

Kayen, R. E., and H. J. Lee (1991), Pleistocene slope instability of gas hydrate-laden sediment on the Beaufort Sea Margin, *Mar. Geotechnol.*, *10*, 125–141, doi:10.1080/10641199109379886.

Kayen, R. E., and H. J. Lee (2002), Slope stability in regions of seafloor gas hydrate: Beaufort Sea continental slope, in *Submarine Landslides: Selected Studies in the US Exclusive Economic Zone*, edited by W. C. Schwab et al., *U.S. Geol. Surv. Bull.*, *2002*, 97–103.

Kiefte, H., M. J. Clouter, and R. E. Gagnon (1985), Determination of acoustic velocities of clathrate hydrates by Brillouin spectroscopy, *J. Phys. Chem.*, *89*, 3103–3108, doi:10.1021/j100260a031.

Kirby, J. M. (1999), Soil stress measurement: Part I. Transducer in a uniform stress field, *J. Agric. Eng. Res.*, *72*, 151–160, doi:10.1006/jaer.1998.0357.

Kvenvolden, K. A., and T. D. Lorenson (2001), The global occurrence of natural gas hydrates, in *Natural Gas Hydrates: Occurrence, Distribution and Detection*, *Geophys. Monogr. Ser.*, *124*, edited by C. K. Paull and W. P. Dillon, pp. 3–18, AGU, Washington, D. C.

Kvenvolden, K. A., G. E. Claypool, C. N. Threlkeld, and E. D. Sloan (1984), Geochemistry of a naturally occurring massive marine gas hydrate, in *Advances in Organic Geochemistry 1983*, edited by P. A. Schenck et al.,703–713, Pergamon, Oxford, U. K.

Lee, M. W., and T. S. Collett (2001), Comparison of elastic velocity models for gas-hydrate-bearing sediments, in *Natural Gas Hydrates: Occurrence, Distribution and Detection*, *Geophys. Monogr. Ser.*, *124*, edited by C. K. Paull and W. P. Dillon, pp. 179–187, AGU, Washington, D. C.

Lee, M. W., and W. F. Waite (2008), Estimating pore-space gas hydrate saturations from well-log acoustic data, *Geochem. Geophys. Geosyst.*, *9*, Q07008, doi:10.1029/2008GC002081.

Lu, H., Y.-T. Seo, J.-W. Lee, I. Moudrakovski, J. A. Ripmeester, N. R. Chapman, R. B. Coffin, G. Gardner, and J. Pohlman (2007), Complex gas hydrate from the Cascadia margin, *Nature*, *445*, 303–306, doi:10.1038/nature05463.

Mavko, G., T. Mukerji, and J. Dvorkin (1998), *The Rock Physics Handbook: Tools for Seismic Analysis in Porous Media*, 329 pp., Cambridge Univ. Press, Cambridge, U. K.

McIver, R. D. (1982), Role of naturally occurring gas hydrates in sediment transport, *AAPG Bull.*, *66*(6), 789–792.

Milkov, A. V. (2005), Molecular and stable isotope compositions of natural gas hydrates: A revised global dataset and basic interpretations in the context of geological settings, *Org. Geochem.*, *36*, 681–702, doi:10.1016/j.orggeochem.2005.01.010.

Nixon, M. F., and J. L. H. Grozic (2007), Submarine slope failure due to gas hydrate dissociation: A preliminary quantification, *Can. Geotech. J.*, *44*, 314–325, doi:10.1139/T06-121.

Northwood, T. D. (1947), Sonic determination of the elastic properties of ice, *Can. J. Res.*, *Sect. A*, *25*, 88–95.

Rawn, C. J., A. J. Rondinone, B. C. Chakoumakos, S. L. Marshall, L. A. Stern, S. Circone, S. Kirby, C. Y. Jones, B. H. Toby, and Y. Ishii (2002), Neutron powder diffraction studies as a function of temperature of sII hydrate formed from a methane+ethane gas mixture, paper presented at 4th International Conference on Gas Hydrates, Heat Transfer Soc. of Jpn., Yokohama, 19–23 May.

Richards, T. W., and C. L. Speyers (1914), The compressibility of ice, *J. Am. Chem. Soc.*, *36*, 491–494, doi:10.1021/ja02180a004.

Röttger, K., A. Endriss, J. Ihringer, S. Doyle, and W. F. Kuhs (1994), Lattice constants and thermal expansion of H_2O and D_2O ice Ih between 10 and 265 K, *Acta Crystallogr.*, *Sect. B*, *50*, 644–648, doi:10.1107/S0108768194004933.

Ruppel, C. (2007), Tapping methane hydrates for unconventional natural gas, *Elements*, *3*, 193–199, doi:10.2113/gselements.3.3.193.

Sassen, R., S. T. Sweet, D. A. DeFreitas, and A. V. Milkov (2000), Exclusion of 2-methylbutane (isopentane) during crystallization of structure II gas hydrate in sea-floor sediment, Gulf of Mexico, *Org. Geochem.*, *31*, 1257–1262, doi:10.1016/S0146-6380(00)00144-3.

Shaw, G. (1986), Elastic properties and equation of state of high pressure ice, *J. Chem. Phys.*, *84*, 5862–5868, doi:10.1063/1.449897.

Shimizu, H., T. Kumazaki, T. Kume, and S. Sasaki (2002), Elasticity of single-crystal methane hydrate at high pressure, *Phys. Rev. B*, *65*, 212102.

Shpakov, V. P., J. S. Tse, C. A. Tulk, B. Kvamme, and V. R. Belosludov (1998), Elastic moduli calculation and instability in structure I methane clathrate hydrate, *Chem. Phys. Lett.*, *282*, 107–114, doi:10.1016/S0009-2614(97)01241-4.

Sloan, E. D., and C. A. Koh (2007), *Clathrate Hydrates of Natural Gases*, 3rd ed., 721 pp., CRC Press, Boca Raton, Fla.

Smith, A., and D. Kishoni (1986), Measurement of the speed of sound in ice, *AIAA J.*, *24*, 1713–1715, doi:10.2514/3.9510.

Stern, L. A., S. H. Kirby, and W. B. Durham (1996), Peculiarities of methane clathrate hydrate formation and solid-state deformation, including possible superheating of water ice, *Science*, *273*, 1843–1848, doi:10.1126/science.273.5283.1843.

Stern, L., S. Kirby, and W. Durham (1998), Polycrystalline methane hydrate: Synthesis from superheated ice, and low-temperature mechanical properties, *Energy Fuels*, *12*, 201–211, doi:10.1021/ef970167m.

Stern, L., S. Kirby, W. Durham, S. Circone, and W. Waite (2000), Laboratory synthesis of pure methane hydrate suitable for measurement of physical properties and decomposition behavior, in *Natural Gas Hydrate in Oceanic and Permafrost Environments*, edited by M. D. Max, pp. 323–348, Kluwer Acad., Dordrecht, Netherlands.

Stern, L. A., S. H. Kirby, S. Circone, and W. B. Durham (2004), Scanning electron microscopy investigations of laboratory-grown gas clathrate hydrates formed from melting ice, and comparison to natural hydrates, *Am. Mineral.*, *89*, 1162–1175.

Subramanian, S., R. A. Kini, S. F. Dec, and E. D. Sloan (2000), Structural transition studies in methane + ethane hydrates using Raman and NMR, in *Gas Hydrates: Challenges for the Future*, edited by G. D. Holder and P. R. Bishnoi, *Ann. N.Y. Acad. Sci.*, *912*, 873–886.

Taylor, J. R. (1997), *An Introduction to Error Analysis*, 2nd ed., 327 pp., Univ. Sci. Books, Sausalito, Calif.

Trehu, A. H., et al. (2004), Three-dimensional distribution of gas hydrate beneath southern Hydrate Ridge: Constraints from ODP Leg 204, *Earth Planet. Sci. Lett.*, *222*, 845–862, doi:10.1016/j.epsl.2004.03.035.

Tse, J. S. (1987), Thermal expansion of the clathrate hydrates of ethylene oxide and tetrahydrofuran, *J. Phys.*, *48*, 543–549.

Waite, W., M. Helgerud, A. Nur, J. Pinkston, L. Stern, and S. Kirby (2000), Laboratory measurements of compressional and shear wave speeds through methane hydrate, in *Gas Hydrates: Challenges for the Future*, edited by G. D. Holder and P. R. Bishnoi, *Ann. N.Y. Acad. Sci.*, *912*, 1003–1010.

Waite, W. F., T. J. Kneafsey, W. J. Winters, and D. H. Mason (2008), Physical property changes in hydrate-bearing sediment due to depressurization and subsequent repressurization, *J. Geophys. Res.*, *113*, B07102, doi:10.1029/2007JB005351.

Whalley, E. (1980), Speed of longitudinal sound in clathrate hydrates, *J. Geophys. Res.*, *85*, 2539–2542, doi:10.1029/JB085iB05p02539.

Whiffen, B. L., H. Kiefte, and M. J. Clouter (1982), Determination of acoustic velocities in xenon and methane hydrates by Brillouin spectroscopy, *Geophys. Res. Lett.*, *9*, 645–648, doi:10.1029/GL009i006p00645.

Willoughby, E. C., K. Latychev, R. N. Edwards, K. Schwalenberg, and R. D. Hyndman (2008), Seafloor compliance imaging of marine gas hydrate deposits and cold vent structures, *J. Geophys. Res.*, *113*, B07107, doi:10.1029/2005JB004136.

Xu, J. (1996), Brillouin scattering and ultrasonic studies at high temperature and high pressure, *Chem. Geol.*, *128*, 17–24, doi:10.1016/0009-2541(95)00160-3.

Yun, T. S., G. A. Narsilio, J. C. Santamarina, and C. Ruppel (2006), Instrumented pressure testing chamber for characterizing sediment cores recovered at in situ hydrostatic pressure, *Mar. Geol.*, *229*, 285–293, doi:10.1016/j.margeo.2006.03.012.

Zha, C.-S., H.-K. Mao, and R. J. Hemley (2000), Elasticity of MgO and a primary pressure scale to 55 GPa, *Proc. Natl. Acad. Sci. U. S. A.*, *97*, 13,494–13,499, doi:10.1073/pnas.240466697.

M. B. Helgerud, ExxonMobil Exploration Company, P.O. Box 4778, Houston, TX 77210-4778, USA.

S. H. Kirby, U.S. Geological Survey, 345 Middlefield Road, MS 977, Menlo Park, CA 94025, USA.

A. Nur, Department of Geophysics, Stanford University, Stanford, CA 94305, USA.

W. F. Waite, U.S. Geological Survey, 384 Woods Hole Road, Woods Hole, MA 02543, USA. (wwaite@usgs.gov)